Graphene microsheets enter cells through spontaneous membrane penetration at edge asperities and corner sites

Yinfeng Li[a,b,1], Hongyan Yuan[a,1], Annette von dem Bussche[c,1], Megan Creighton[a], Robert H. Hurt[a,d,2], Agnes B. Kane[c,d,2], and Huajian Gao[a,d,2]

[a]School of Engineering, Brown University, Providence, RI 02912; [b]Department of Engineering Mechanics, Shanghai Jiao Tong University, Shanghai 200240, China; [c]Department of Pathology and Laboratory Medicine, Brown University, Providence, RI 02912; and [d]Institute for Molecular and Nanoscale Innovation, Brown University, Providence, RI 02912

Edited* by L. B. Freund, University of Illinois at Urbana–Champaign, Urbana, IL, and approved June 13, 2013 (received for review December 27, 2012)

Understanding and controlling the interaction of graphene-based materials with cell membranes is key to the development of graphene-enabled biomedical technologies and to the management of graphene health and safety issues. Very little is known about the fundamental behavior of cell membranes exposed to ultrathin 2D synthetic materials. Here we investigate the interactions of graphene and few-layer graphene (FLG) microsheets with three cell types and with model lipid bilayers by combining coarse-grained molecular dynamics (MD), all-atom MD, analytical modeling, confocal fluorescence imaging, and electron microscopic imaging. The imaging experiments show edge-first uptake and complete internalization for a range of FLG samples of 0.5- to 10-μm lateral dimension. In contrast, the simulations show large energy barriers relative to k_BT for membrane penetration by model graphene or FLG microsheets of similar size. More detailed simulations resolve this paradox by showing that entry is initiated at corners or asperities that are abundant along the irregular edges of fabricated graphene materials. Local piercing by these sharp protrusions initiates membrane propagation along the extended graphene edge and thus avoids the high energy barrier calculated in simple idealized MD simulations. We propose that this mechanism allows cellular uptake of even large multilayer sheets of micrometer-scale lateral dimension, which is consistent with our multimodal bioimaging results for primary human keratinocytes, human lung epithelial cells, and murine macrophages.

molecular dynamics simulation | graphene-cell interaction | lipid membrane | edge cutting | corner penetration

Graphene is a 2D plate-like material consisting of a single layer of hexagonally arranged carbon atoms with extraordinary electrical (1), mechanical (2), and thermal properties (3). Bilayer, trilayer (4), few-layer graphene, and multilayer structures with thickness <100 nm are closely related nanomaterials that are often manufactured by thermal exfoliation of graphite and often exist as dry powders during processing (5), which increases the probability of workplace exposure. For the purposes of this article, we refer to this set of structures as "graphene-family nanomaterials" (GFNs) (6). Many GFNs have aerodynamic diameters less than 5 μm and thus fall into the category of potentially respirable materials. Even GFNs with large lateral dimensions (>20 μm) typically fall in the potentially respirable range, and for these the large lateral dimension presents challenges for macrophage-mediated clearance, raising the possibility of long residence times in the lung (7). Workplace measurements and laboratory simulations have documented the potential for human inhalation exposure to engineered nanomaterials during several steps in manufacturing processes (8). In addition to inhalation of dry powders, carbon-based nanomaterials can become airborne during sonication of particles in suspension (9) and during cutting or drilling of composites. In addition to occupational exposures, GFNs may be deliberately implanted or injected for biomedical applications that include biosensors (10), tissue scaffolds (11, 12), carriers for drug delivery (13, 14) or gene therapy (15), antibacterial agents (16), and bioimaging probes (17, 18). The large specific surface area of graphene allows high-density biofunctionalization or drug loading (19, 20) and more efficient tumor targeting capability (13), and graphene may also offer lower toxicity and better manufacturing reproducibility than some other material platforms (18, 21).

The lateral dimensions of GFNs span orders of magnitude, from 10 nm to >100 μm (larger than most target cells), and the maximum dimensions of a nanomaterial are important for cell uptake, renal clearance, blood–brain barrier transport, and many other biological phenomena. Graphene-based sheets of small lateral dimension (<100 nm) are being developed for drug delivery and diagnostic applications. These "nanosheets" have been observed to enter cells (6, 13–15, 17, 18) and their membrane translocation has been studied experimentally (22) and through simulation (23, 24). Titov and coworkers conducted coarse-grained molecular dynamics simulations to study the interaction of small graphene and few-layer graphene (FLG) nanosheets with a lipid bilayer and reported stable graphene–lipid hybrid structures (23). Guo et al. studied the translocation of small graphene nanosheets across lipid bilayers and their effects on membrane deformation (24). Much less is known about the fundamental cellular interactions of graphene materials with micrometer-scale lateral dimension (graphene microsheets) that are a main thrust in current graphene materials development. The urgency to develop guidelines for manufacturing safer biomedical diagnostics and therapies (6, 18), as well as regulating occupational and environmental exposure (25, 26), justifies significant efforts to clarify the mechanisms of cell membrane interaction with carbon nanomaterials and with graphene microsheets in particular.

Previous studies of carbon nanotubes entering the cell membrane have suggested that there exists a critical structural dimension on the order of the bilayer thickness (around 4 nm), below which direct penetration into the bilayer becomes possible and above which receptor-mediated endocytosis is needed for the uptake (27–29). Graphene is atomically thin in one dimension, but typically large in two other dimensions, and our preliminary modeling work showed large energy barriers for membrane penetration even when monolayer sheets encounter the lipid bilayer edge-first. The entry barriers were found to

Author contributions: Y.L., H.Y., A.v.d.B., R.H.H., A.B.K., and H.G. designed research; Y.L., H.Y., and A.v.d.B. performed research; M.C. contributed new reagents/analytic tools; Y.L., H.Y., A.v.d.B., R.H.H., A.B.K., and H.G. analyzed data; and Y.L., H.Y., A.v.d.B., R.H.H., A.B.K., and H.G. wrote the paper.

The authors declare no conflict of interest.

*This Direct Submission article had a prearranged editor.

[1]Y.L., H.Y., and A.v.d.B. contributed equally to this work.

[2]To whom correspondence may be addressed. E-mail: Huajian_Gao@brown.edu, robert_hurt@brown.edu, or Agnes_kane@brown.edu.

This article contains supporting information online at www.pnas.org/lookup/suppl/doi:10.1073/pnas.1222276110/-/DCSupplemental.

be even larger for multilayer graphene materials, which are of particular interest in our study due to large-scale manufacturing by exfoliation. It was unclear at the preliminary stage which types of graphene materials (what range of layer numbers and lateral dimensions) would be capable of cell entry and by what biophysical mechanism. We therefore conducted a coupled experimental and computational study of graphene–membrane interactions, using molecular dynamics and in vitro cell imaging with emphasis on the geometry and dynamics of cell penetration and uptake. The simulations use similar coarse-graining methods to those in our previous study for the tip entry of carbon nanotubes and related 1D materials (30), but require higher spatial resolution due to the atomic thickness of graphene. We investigate the atomic-scale mechanisms of cell interaction with few-layer graphene microsheets via coarse-grained molecular dynamics (CGMD) and all-atom steered molecular dynamics (SMD) simulations. The CGMD simulations illustrate the dynamic process of graphene–bilayer interaction, whereas the SMD simulations allow us to determine the energy barriers associated with initial graphene penetration. SMD simulations predict that idealized graphene sheets with smooth edges will not penetrate lipid bilayers at room temperature due to high energy barriers, even in cases where the initial encounter is strictly edge-on. Examination of actual fabricated graphene microsheets reveals highly irregular edge topographies, and we therefore develop a separate theoretical treatment of graphene–bilayer interaction initiated at sharp corners or protrusions. This latter model predicts that cell uptake can be initiated by a spontaneous localized piercing of the membrane at corners or asperities followed by spontaneous propagation along the graphene edge to achieve full penetration. These new model predictions are validated by confocal fluorescence bioimaging and electron microscopy, which show edge-first or corner-first membrane penetration and complete cellular internalization for a range of few-layer graphene microsheets and three cell types.

Results and Discussion

Coarse-Grained Molecular Dynamics. Fig. 1 shows the CGMD results for graphene and few-layer graphene interacting with lipid bilayers. In the first simulation set, a small, rhombic, monolayer graphene flake with edge length of 6.4 nm is placed initially at a distance about 4 nm above and parallel to a square patch of lipid bilayer with 992 lipid molecules and 67,817 water molecules in a cubic box with edge dimension 24 nm (Fig. 1*A*). Periodic boundary conditions are imposed in all three dimensions. Under thermal fluctuations, the graphene flake undergoes Brownian motion, including rapid vibration, rotation, and migration in the vicinity of the bilayer. Spontaneous piercing into the bilayer is observed to begin as soon as the flake finds a configuration with one of its sharpest corners oriented nearly orthogonal to the membrane (Fig. 1 *B* and *C*). Piercing is facilitated by the attractive interactions between graphene and the tail groups of lipids, but occurs only after the tip of the penetrating corner touches the hydrophobic core of the bilayer. In our CG simulations, the lipid membrane can be fully penetrated through by the graphene flake, accompanied by the tilt of the graphene flake to maximize its coverage with the membrane interior. The small graphene flake in our simulation eventually ends up embedded in the bilayer due to its small dimensions (Movie S1). The simulation of a rhombic graphene flake with two different corner angles (30°and 60°) demonstrates that orthogonal piercing of the sharpest corner of graphene has the lowest energy barrier and is the most preferred entry pathway. The edge planes of graphene have a complex chemistry and are typically decorated with hydrophilic oxygen functional groups, whereas in cell culture medium graphene may exhibit adsorbed proteins that can also reduce apparent hydrophobicity. The set of GFN samples used in our bioimaging studies has C/O ratios ranging from 10 to 32 by X-ray photoelectron spectroscopy (31) with the oxygen atoms presumed to be on edge and defect sites. Also, the amount of adsorbed protein was measured to cover 3–46% of the GFN surface area, depending on conditions and sample (*SI Text*). To investigate these effects, further CGMD simulations of bilayer interaction with graphene flakes of different shapes and surface chemistry (different corner/edge functionalizations and hydrophilic/hydrophobic properties) confirm that small graphene sheets tend to penetrate into the cell via spontaneous piercing at their sharpest hydrophobic corner. A series of calculations with different interaction parameters between graphene and lipid molecules are also performed to demonstrate that the corner entry mode is robust within a broad range of dissipative particle dynamics (DPD) parameters (*SI Text*). We will show shortly that the nearly orthogonal orientation of a sharp graphene corner with respect to the bilayer minimizes their interactive free energy and is the thermodynamically preferred configuration even before penetration begins.

We also performed CGMD simulations of large few-layer graphene sheets interacting with lipid bilayers (Fig. 1 *F–H*). We began by studying an ideal, atomically smooth, infinite graphene edge interacting with lipid bilayers, but did not observe penetration (*SI Text*, Fig. S6*A*, and *Discussion*). We realized that the edges of experimentally fabricated graphene exhibit atomic-scale roughness (Fig. 1*E*) as seen by atomically resolved scanning tunneling microscopy (32–34), and most few-layer graphene sheets also show very rough edges (see Fig. 4), as well as terraced or beveled edge structures that become successively thinner toward one of the two faces (35, 36). Fig. 1*F* shows a model terraced edge structure created on a five-layer FLG flake interacting with a bilayer. The simulation system consists of a patch of bilayer with 2,016 lipid molecules and 133,052 water molecules in a cubic box with dimensions of 24 nm × 48 nm × 24 nm. The plate-like FLG, which has a ragged edge topography mimicking those observed in experiments, is composed of five atomic layers with an equilibrium interlayer distance of 0.34 nm and placed initially at a distance about 3 nm above and orthogonal to the bilayer. Each graphene layer is assigned a different color. The first two and last two layers are set to be symmetrical with respect to the midlayer. To mimic part of a much larger structure for which Brownian motion is limited, the top edge of the FLG is clamped and periodic boundary conditions are imposed in all three dimensions of the simulation box. The lipid bilayer undergoes Brownian motion in the vicinity of the large graphene edge for 2.19 μs under the confinement of a harmonic potential. The latter is then removed and the bilayer membrane is set free to interact with the ragged graphene edge.

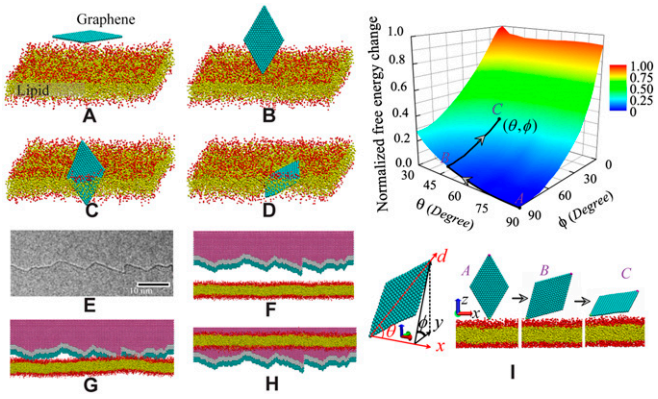

Fig. 1. (*A–H*) Coarse-grained molecular dynamics simulations of interactions between a lipid bilayer and (*A–D*) a small graphene flake or (*E–H*) a large five-layer graphene sheet with staggered stacking and roughened edge topography. (*I*) The normalized free energy of the system as a function of the graphene orientation when one of the sharpest corners is fixed at a distance of 0.5 nm above the bilayer. Note that *A–D* and *F–H* are time sequences; *E* is an experimental graphene edge structure (34–36).

It is seen that the FLG penetrates the bilayer despite its size, starting with localized piercing at sharp protrusions along the edge. The penetrated portion of the membrane then propagates along the whole edge, resulting in full penetration (Movie S2). In this process, the energy barrier to penetration is overcome by local piercing at sharp corners along the nominally flat edge, and the full penetration is driven by the attractive interaction between the graphene and the tail groups of lipids once initial piercing is successful. We have tested the robustness of this entry mode by carrying out further CGMD simulations on monolayer or few-layer graphene flakes with an isolated protrusion or a terrace or by initiating contact near a corner or a locally folded edge (*SI Text* and Figs. S2–S7). The simulation results all show similar pathways that are initiated by localized piercing at an atomically thin graphene feature, which requires only thermal energy to overcome the small barrier, followed by spreading and complete penetration driven by hydrophobic forces between the graphene and the bilayer core. We believe this entry mechanism may be generic for cell uptake of all 2D hydrophobic nanomaterials with atomic-scale thickness. The importance of localized corner piercing for entry initiation can also be demonstrated by carrying out simulations on ideal, atomically smooth, infinite graphene edges without the irregular features observed in real samples. In this case, our simulations show that the lipid bilayer is repelled away from the graphene edge due to a combination of a strong entry energy barrier and entropic interactions between the bilayer and an atomically smooth graphene edge (*SI Text* and Fig. S6*A*). This last simulation was done to further demonstrate the importance of local piercing as the initiating event, but does not correspond to any known biological exposure scenario, because it would require cell contact with a uniform, atomically smooth, horizontally aligned, long-length graphene edge structure that is difficult to achieve in practice.

Our simulations demonstrate local orthogonal piercing at a sharp corner or asperity that initiates graphene penetration of lipid bilayers. To better understand this behavior, we use the thermodynamic integration (TI) technique (37) to calculate the free energy of the system as a function of two orientation angles (θ, ϕ) of a rhombic graphene flake when one of the sharp corners of the flake is fixed at a distance of 0.4 nm above the bilayer (the detailed implementation of the TI method is given in *SI Text*). Here θ is the angle between the long diagonal axis of the flake and the bilayer within the graphene plane and ϕ is the angle between the vectors normal to the graphene plane and the membrane plane (Fig. 1*I*). The free energy associated with orthogonal corner piercing $(90°, 90°)$ is set to 0 as a reference value. Not surprisingly, the orientation $(30°, 0°)$, which corresponds to the graphene flake parallel to the bilayer plane, shows the highest free energy because it induces the most severe confinement of thermal motion in this configuration. We further normalized the calculated free energy by its peak value at the parallel configuration $(30°, 0°)$. The plotted normalized free energy in Fig. 1*I* demonstrates that the orthogonal orientation $(90°, 90°)$ exhibits the lowest free energy due to its weakest confinement on the thermal motions of both membrane and graphene (thereby maximizing the entropy of the system).

All-Atom Simulations. Our CGMD simulations suggest that localized corner piercing plays a critical role during the initial stage of cell uptake of graphene. To determine the energy evolution associated with such initial piercing events, further simulations are conducted on an all-atom model of corner piercing of a monolayer graphene flake across a bilayer patch of 1-palmitoyl-2-oleoyl-sn-glycero-3-phosphocholine (POPC) lipid in a box of water molecules. The all-atom simulations are of two types. Type I simulations are designed to test whether there exists a positive driving force for piercing in an all-atom MD simulation. As shown in Fig. 2*A*, a triangular graphene flake initially placed in a corner-piercing configuration across the bilayer was observed to spontaneously move downward, penetrating further into the bilayer (Movie S3). In type II simulations, the energy barrier associated with corner piercing is calculated by SMD simulations (38), in which a graphene corner is pulled across the bilayer by a virtual spring (see *SI Text* for more details). Fig. 2*B* shows the graphene–bilayer interaction energy calculated from the SMD simulations as a function of the penetration distance. The SMD calculations confirm that the energy barrier is small, only $\sim 5k_BT$, for the graphene corner to pierce through the top hydrophilic head region of the bilayer. Shortly after this point, the total interaction energy starts to decrease due to favorable interactions between the lipid tails in the core of the bilayer and an ever-increasing area of immersed graphene. Thus, both our CGMD and all-atom simulations reveal that corner piercing involves a small energy barrier comparable to thermal energy and is essentially a spontaneous process.

Both CGMD and all-atom simulations indicate that the lipid bilayer structure remains essentially intact upon graphene insertion except that the hydrophobic tails of lipids are somewhat straightened due to strong adhesion onto the side surfaces of graphene. In a continuum description, the energy change accompanying piercing can be expressed in terms of four variables: h_H and h_T (thicknesses of the head and tail groups in the lipid monolayer, as shown in Fig. 2*C*) and γ_H and γ_T (interaction energy densities between one side surface of graphene and head and tail groups of lipids relative to that between solvent and graphene). For a graphene corner with an internal angle of 2α, the rate of energy change during piercing can then be written as a piecewise function of the penetration depth h as (*SI Text*)

$$\frac{\partial E}{\partial h} = \begin{cases} 4h\gamma_H \tan\alpha & 0 < h \le h_H \\ 4[h_H\gamma_H + (h-h_H)\gamma_T]\tan\alpha & h_H < h \le h_H + 2h_T \\ 4[(h-2h_T)\gamma_H + 2h_T\gamma_T]\tan\alpha & h_H + 2h_T < h \le 2h_H + 2h_T \\ 8(\gamma_H h_H + \gamma_T h_T)\tan\alpha & 2h_H + 2h_T < h. \end{cases} \quad [1]$$

Our all-atom simulation shown in Fig. 2*A* indicates that there is a positive driving force for the last regime of piercing, i.e., $\gamma_H h_H + \gamma_T h_T < 0$. Under this condition, it can be seen that the energy increases in the first regime, $0 < h \le h_H$, but decreases in

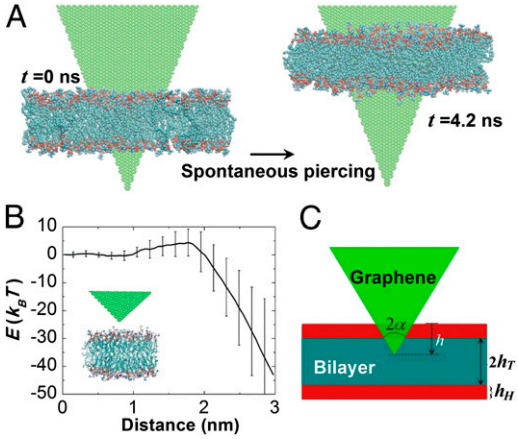

Fig. 2. All-atom molecular dynamics simulations of corner piercing of a monolayer graphene across a lipid bilayer. (*A*) Simulations directly showing that the corner piercing proceeds spontaneously. (*B*) Graphene–bilayer interaction energy as a function of the penetration distance, showing the existence of an energy barrier of about $5k_BT$ associated with corner piercing. The mean value of interaction energy is obtained from 11 independent simulation runs and the error bars show SD. The relatively large fluctuations of interaction energy at large penetration distance are mainly due to random translational and rotational movements of graphene relative to the bilayer membrane and random configurational changes of individual lipids adjacent to the graphene. (*C*) Analytical model of corner piercing.

both regimes $h_H + 2h_T < h \leq 2h_H + 2h_T$ and $2h_H + 2h_T < h$. The energy peak occurs when the graphene tip lies in the hydrophobic core, $h_H < h \leq h_H + 2h_T$, at a point defined by $dE/dh = 0$. This gives the energy barrier for piercing as $E_{barrier} = 2(1 - \gamma_H/\gamma_T) h_H^2 \gamma_H \tan\alpha$ at a critical penetration depth of $h_{cr} = (1 - \gamma_H/\gamma_T) h_H$.

The surface interaction energy densities γ_H and γ_H may be estimated as $\gamma_H = 7k_BT \cdot \text{nm}^{-2}$, $\gamma_H = -7k_BT \cdot \text{nm}^{-2}$ if they are considered to be of the same order of magnitude as those between the hydrocarbon tail groups and water (39). Taking $h_H = 0.5$ nm and $\alpha = 45°$ shows that the energy barrier for corner piercing is $E_{barrier} = 2(1 - \gamma_H/\gamma_T) h_H^2 \gamma_H \tan\alpha \approx 7k_BT$ at a critical penetration depth of $h_{cr} = (1 - \gamma_H/\gamma_T) h_H \approx 1.0$ nm. These numbers are in excellent agreement with the direct SMD simulation results shown in Fig. 2*B*.

It may be tempting to make an analogy between graphene corner piercing into a lipid bilayer described here and mechanical piercing by stress concentration at sharp corners. However, we emphasize that the former is an essentially spontaneous process, whereas the latter is driven by an applied force.

Bioimaging Experiments. Figs. 3 and 4 present confocal fluorescent and ex situ electron micrographs that confirm the MD predictions of edge/corner-first penetration and cell entry of few-layer graphene microsheets. Lung epithelial cells and keratinocytes are representative of the epithelial lining of the respiratory tract and the skin, respectively (40), and form flat, single-cell monolayers in vitro (Fig. 3). Polarized epithelial cells have a well-organized microtubular cytoskeletal network whereas macrophages have a subcortical distribution of actin filaments that can be visualized using indirect immunofluorescence confocal microscopy (Fig. 3 *A*–*C*, *Insets*). Plate-like graphene microsheets are internalized by human lung epithelial cells (Fig. 3 *A* and *B*) and macrophages (Fig. 3*C*) and can be visualized within the cytoplasm using confocal imaging. It is interesting that the graphene basal planes show preferential orientation parallel to the basolateral cell surface attached to the substrate. Plate-like graphene microsheets physically disrupt the cytoskeletal organization of both lung epithelial cells (Fig. 3 *A* and *B*) and macrophages (Fig. 3*C*). In thin sections using transmission electron microscopy (TEM), some graphene microsheets can be visualized within cytoplasmic vacuoles inside macrophages (Fig. 3*D*) and lung epithelial cells (Fig. 3*E*). The overall structure and integrity of subcellular organelles are preserved as revealed by TEM (Fig. 3 *D* and *E*), confirming our in vitro assays that show preserved cell viability (*SI Text* and Fig. S8).

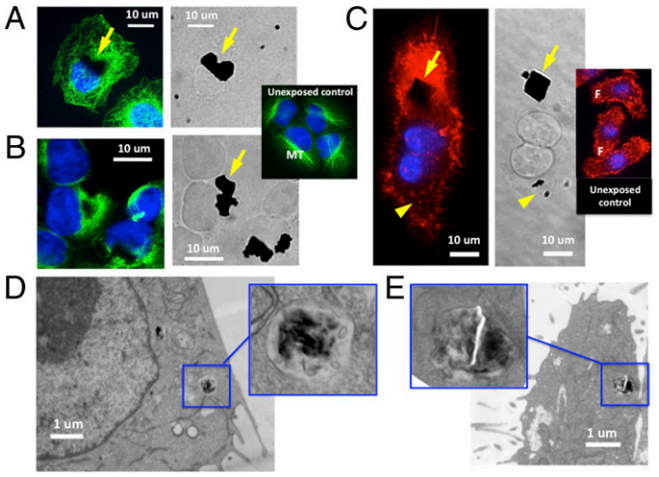

Fig. 3. Cellular uptake and internalization of few-layer graphene microsheets. (*A*–*C*) Confocal images of human lung epithelial cells (*A* and *B*) and mouse macrophages (*C*) exposed to graphene microsheets (0.5- to 25-μm lateral dimension) after 24 h and 5 h, respectively. The nuclei in *A* and *B* are visualized (blue fluorescence) with 4′,6-diamidino-2-phenylindole (DAPI). The microtubules of the lung epithelial cells (*A* and *B*) are visualized using antitubulin beta antibodies conjugated with FITC (green fluorescence), whereas the actin cytoskeleton of macrophages shown in *C* is visualized using rhodamine–phalloidin (red fluorescence). In unexposed lung epithelial cells (*A* and *B*, *Inset*), cytoplasmic microtubules (MT) form a linear network spanning across the cytoplasm. Internalized graphene flakes (yellow arrows, *A* and *B*) physically displace the linear microtubular network. In unexposed macrophages (*C*, *Inset*), filamentous actin (F) is organized into aggregates beneath the plasma membrane. Internalized graphene flakes with large lateral dimension (yellow arrow, *C*) induce dense aggregates of actin filaments whereas submicron graphene sheets (yellow arrowhead, *C*) do not disrupt the actin cytoskeleton. Transmission electron micrographs of macrophages (*D*) and lung epithelial cells (*E*) exposed to 10 ppm FLG sheets (~800 nm in lateral dimension) for 5 h and 24 h show localization in the cytoplasm within membrane-bound vacuoles (blue *Insets*). Graphene microsheets inside vacuoles appear as electron-dense linear sections (*D*, *Inset*) or irregular flakes (*E*, *Inset*).

The imaging protocols used in Fig. 3 are useful to show graphene internalization and orientation, but do not reveal the entry mode. We therefore carried out shorter time exposures to capture the uptake process, using ex situ field-emission SEM of target cells with the outer membrane enhanced by osmium tetroxide postfixation. This imaging was carried out both with and without critical point drying to check for drying artifacts. Fig. 4 shows high-resolution images of cell surfaces exposed to graphene after 5 or 24 h. Edge-first or corner-first penetration of the membrane is seen in all cases and for all three target cell types. Fig. 4 *C* and *D* shows particularly clear cases of membrane penetration that appears to have initiated at an asperity or protrusion on the graphene edge (Fig. 4*C*) or initiated at a graphene corner (Fig. 4*D*). Note that the edges of these sheets are observed to be highly irregular (Fig. 4 *A*, *C*, and *D*) and provide numerous sites for initial penetration as described in the modeling (*SI Text* and Fig. S9). Internalization of these plate-like graphene microsheets ranging in lateral dimension from 0.5 nm up to 5 μm (Table S1) did not compromise cell viability at the doses and time points used in these in vitro studies. More generally, however, inhaled nanoparticles can be associated with adverse health effects (41) and Schinwald et al. (7) reported that graphene nanoplatelets induced granuloma formation and lung inflammation following pharyngeal aspiration in mice. Intracellular uptake and cytoplasmic localization of plate-like graphene nanomaterials may interfere with cytoskeleton organization (Fig. 3 *A*–*C*) and normal physiological functions including polarized secretion (40), barrier formation (42), and cell migration during differentiation and repair of epithelial injury (43). Internalization of nanoparticles by macrophages has been shown to disrupt phagocytosis and clearance of particles and microbes from the lungs (44, 45). Schinwald et al. (7) provide evidence that graphene nanoplatelets are not readily cleared from the lungs and induce release of proinflammatory mediators from macrophages. Other studies report that graphene nanomaterials are biocompatible (46, 47), and much more work is needed before graphene material health risks can be fully assessed.

In summary, coarse-grained molecular dynamics, all-atom steered MD, analytical modeling, and live-cell and ex situ bioimaging were used to investigate the fundamental mechanisms of graphene interactions with lipid bilayers. The simulations reveal direct bilayer penetration that begins with localized piercing at sharp corners or at protrusions along graphene edges followed by propagation along the edge to achieve full penetration. For a small graphene flake, Brownian motion and entropic driving forces in the near-membrane region first position the flake orthogonal to the bilayer plane, which then leads to spontaneous corner piercing. All-atom steered molecular dynamics simulations track the free energy evolution during corner piercing and reveal only a small energy barrier, comparable to k_BT. Interestingly, in the absence of sharp corners or edge protrusions, the cell membrane has a high intrinsic energy barrier against penetration by long graphene edge segments even though they are atomically thin. Such uniform, atomically smooth, horizontally

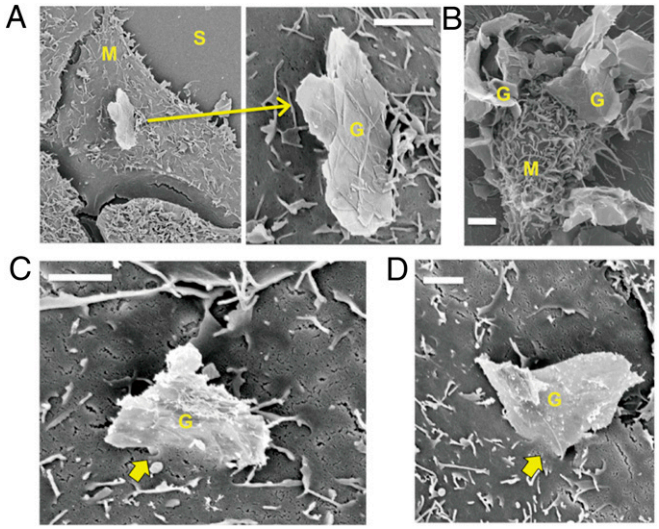

Fig. 4. Cell membrane interactions with graphene microsheets, showing edge or corner penetration for each of three cell types. (*A*) Corner penetration observed for a graphene sheet of micrometer-scale lateral dimension on the surface of a human lung epithelial cell at low and high magnification. (*B*) Edge penetration of multiple microsheets (G) into a macrophage (M). (*C*) Edge penetration for a 5-μm sheet interacting with primary human keratinocytes, in which the edge entry appears to have been nucleated at an asperity or protrusion (thick yellow arrow). (*D*) Corner penetration mode at the surface of a primary human keratinocyte. The tilted, upright orientation of the graphene sheet produces subtle e-beam shadows immediately adjacent to the sheet in some images. Highly irregular edge topography is seen on essentially all graphene sheets. All images are field-emission scanning electron micrographs of fixed cells with osmium tetroxide postfixation. Exposure times are 24 h except for that of macrophages, which is a 5-h exposure. Cells in *A* and *B* were not subjected to critical point drying during sample preparation for scanning electron microscopy. The graphene microsheets here and in Fig. 3 have layer numbers that range from 4 to 25. (Scale bars, 2 μm.)

aligned, long-length graphene edges are rare, however, so in practice cell penetration is spontaneous due to the presence of atomic- or nano-scale edge roughness that essentially eliminates the energy barrier. Experimental imaging studies confirm graphene penetration of cell membranes in a dominant edge-first or corner-first mode for each of three cell types studied: lung epithelial cells, keratinocytes, and macrophages. The experiments also show penetration and successful uptake of GFN flakes as large as 5–10 μm in lateral dimension, which supports the model prediction that penetration activation barriers are not intrinsically length dependent, because of initiation at local sharp features. Once the initial energy barrier for spontaneous membrane penetration has been overcome, we hypothesize that interaction between the hydrophobic basal surfaces of graphene microsheets with the inner hydrophobic region of the plasma membrane promotes cellular uptake. Hydrophobic surfaces are considered to represent damage-associated molecular patterns (DAMPs) that nonspecifically activate the innate immune response (48). Hydrophobic cellular surfaces (49) and surface functionalized nanoparticles (50) are more readily internalized and initiate more potent innate immune responses than weakly charged, hydrophilic surfaces. By this mechanism, we hypothesize that graphene microsheets that penetrate into hydrophobic lipid domains may be recognized as DAMPs by target cells that are the first line of defense against particles and microbes deposited on the skin or on the epithelial lining of the lungs following inhalation. The ability of graphene microsheets with large lateral dimension to penetrate and enter cells, documented here both experimentally and through simulation, may lead to cytoskeletal disruption, impaired cell motility, compromised epithelial barrier function, or other geometric and steric effects that deserve further study.

Materials and Methods

Coarse-Grained MD Simulations. The coarse-grained simulations in this paper are based on DPD, which is a Lagrangian method derived from coarse graining of molecular dynamics (51) widely used as a mesoscopic simulation method for biomembrane systems (52–55). The lipid bilayer membrane is represented by the $H_3(T_5)_2$ coarse-grained model (*SI Text* and Fig. S1) (51). The hydrophilic lipid heads and hydrophobic lipid tails are shown as red and yellow beads, respectively. A unit cell of CG graphene consists of three beads with the nearest-neighbor distance of 0.4 nm and internal angle of 60°. The interactions among the beads are chosen to keep elastic properties of CG graphene consistent with experimental results (2, 56). The interaction parameters between graphene and lipid molecules are calibrated against parameters from all-atom MD simulations and also varied in a range to test the robustness of key observations. The simulations are performed in the number-volume-temperature (NVT) ensembles with the time step taken as $\Delta t = 0.003\tau$ and carried out by using the software package LAMMPS (57). More details of the method are given in *SI Text*.

All-Atom MD Simulations. The all-atom MD simulations were performed in NAMD (58) and visualized in VMD (59). The graphene and the POPC lipid bilayer membrane were generated using VMD Graphene Builder and Membrane Builder, respectively. The graphene and lipid bilayer system was then fully hydrated (adding water molecules), using VMD. The CHARMM36 force field (60) with added parameters for the graphene and TIP3 water model was adopted in the simulations. The simulations were composed of two equilibration steps and one production step. Because the lipid membranes generated by the membrane plug-in of VMD were far from the equilibrium state, an equilibrium run of 0.5 ns was carried out in which everything except lipid tails was fixed. This first step allowed the lipid tails to melt into a fluid-like configuration. In the second step, the systems were equilibrated for about 2 ns in the number-pressure-temperature (NPT) ensemble at temperature of 310 K and pressure of 1 atm. Next, the production runs were performed as the third step. In all three steps of simulation, the out-of-plane degrees of freedom of the carbon atoms of the graphene flakes were restricted using harmonic constraints. Further details of the all-atom simulations are given in *SI Text*.

Bioimaging Experiments. Experiments were conducted on three cell types: murine macrophages, lung epithelial cells, and primary human keratinocytes. The cells were exposed to commercial few-layer graphene microsheet samples with a range of lateral dimensions (0.5–10 μm) and layer numbers (4–25). The FLG samples were dispersed using 1,2-dipalmitoyl-sn-glycero-3-phosphocholine (DPPC) (Avanti Polar lipids)/albumin before addition into cell culture medium (Fig. S10). One hundred microliters of graphene flakes in a 5-mg/mL ethanol stock solution were added to 62 μL of a 40-mg/mL DPPC/ethanol solution and vortexed for 5 s followed by addition of 838 μL PBS containing 2% (vol/vol) albumin to produce a 500 μg/mL (ppm) graphene stock solution containing 2.5 mg DPPC and 2% albumin/PBS. The amount of adsorbed protein that results from application of this protocol was measured in separate control experiments and found to comprise 3–46% of the GFN surface area, depending on conditions and sample (*SI Text*). For keratinocytes, the graphene stock solution was diluted to 10 μg/mL graphene in dermal cell basal medium containing keratinocyte growth supplements, whereas RPMI 1640 served as a dilution medium for macrophages and lung epithelial cells. Further details of the cultivation of three cell types are given in *SI Text*.

Confocal fluorescence microscopy. Lung epithelial cells were exposed to graphene flakes for 24 h. The cells were washed and stained with antitubulin antibody conjugated with fluorescein isothiocyanate (FITC) (Cell Signaling; 3623S) and 4′,6-diamidino-2-phenylindole (DAPI). Macrophages were exposed to graphene for 5 h as described above. The cells were washed and stained with rhodamine-conjugated phalloidin and DAPI. Images were visualized using a spinning-disk Olympus confocal fluorescence (Model IX81) motorized inverted research microscope to assess uptake and cytoskeletal organization.

Electron microscopy. For TEM sample preparation two different methods were used to verify that graphene flakes are taken up by the cells. Cells were fixed in Karnovsky's fixative [5% (vol/vol) glutaraldehyde, 4% (vol/vol) formaldehyde in 0.1 M sodium cacodylate buffer, pH 7.4] (Electron Microscopy Sciences; 11650) at 4 °C and then rinsed three times with 0.1 M sodium cacodylate buffer and postfixed in 2% (vol/vol) aqueous osmium tetroxide

(Electron Microscopy Sciences; RT 19152). Samples were dehydrated in ice-cold, graded ethanol solutions and then in ice-cold anhydrous acetone. Infiltration of specimens was achieved using Durcupan ACM resin (Electron Microscopy Sciences) with decreasing proportions of acetone and finally Durcupan alone. Cells were embedded in Durcupan and polymerized at 60 °C for 48 h. Cell blocks were thin sectioned at 80 nm on a Reichert Ultracut Ultramicrotome with either a diamond knife (untreated cells) or a glass knife. Sections were placed on copper grids and viewed on a Philips 410 transmission electron microscope equipped with an Advantage HR CCD camera. Images were acquired with Advanced Microscopy Techniques imaging software. Intracellular localization of graphene nanosheets was also confirmed by sectioning cells grown in monolayer on glass coverslips. For scanning electron microscopy, cells were postfixed in 2% (vol/vol) aqueous osmium tetroxide for 30 min followed by dehydration in 25% (vol/vol), 50% (vol/vol), 70% (vol/vol), 2 × 95% (vol/vol), and 3 × 100% (vol/vol) ethanol. After critical point drying according to the manufacturer's directions (Ladd Research), the coverslips were sputter coated with gold and viewed using field-emission SEM (LEO 1530-VP). More details of the method are given in *SI Text*.

ACKNOWLEDGMENTS. Technical assistance was provided by Paula Weston, Ashish Jachack, Paulette Ferland, and Dr. Charles Vaslet. This work was supported by the National Science Foundation (Grants CMMI-1028530 and CBET-1132446) and the Superfund Research Program of the National Institute of Environmental Health Sciences (Grant P42 ES013660).

1. Zhang Y, Tan Y-W, Stormer HL, Kim P (2005) Experimental observation of the quantum Hall effect and Berry's phase in graphene. *Nature* 438(7065):201–204.
2. Lee C, Wei X, Kysar JW, Hone J (2008) Measurement of the elastic properties and intrinsic strength of monolayer graphene. *Science* 321(5887):385–388.
3. Balandin AA, et al. (2008) Superior thermal conductivity of single-layer graphene. *Nano Lett* 8(3):902–907.
4. Shih C-J, et al. (2011) Bi- and trilayer graphene solutions. *Nat Nanotechnol* 6(7): 439–445.
5. Huang X, et al. (2011) Graphene-based materials: Synthesis, characterization, properties, and applications. *Small* 7(14):1876–1902.
6. Sanchez VC, Jachak A, Hurt RH, Kane AB (2012) Biological interactions of graphene-family nanomaterials: An interdisciplinary review. *Chem Res Toxicol* 25(1):15–34.
7. Schinwald A, Murphy FA, Jones A, MacNee W, Donaldson K (2012) Graphene-based nanoplatelets: A new risk to the respiratory system as a consequence of their unusual aerodynamic properties. *ACS Nano* 6(1):736–746.
8. Kuhlbusch TA, Asbach C, Fissan H, Göhler D, Stintz M (2011) Nanoparticle exposure at nanotechnology workplaces: A review. *Part Fibre Toxicol* 8(1):22.
9. Johnson DR, Methner MM, Kennedy AJ, Steevens JA (2010) Potential for occupational exposure to engineered carbon-based nanomaterials in environmental laboratory studies. *Environ Health Perspect* 118(1):49–54.
10. Kuila T, et al. (2011) Recent advances in graphene-based biosensors. *Biosens Bioelectron* 26(12):4637–4648.
11. Kalbacova M, Broz A, Kong J, Kalbac M (2010) Graphene substrates promote adherence of human osteoblasts and mesenchymal stromal cells. *Carbon* 48(15): 4323–4329.
12. Nayak TR, et al. (2011) Graphene for controlled and accelerated osteogenic differentiation of human mesenchymal stem cells. *ACS Nano* 5(6):4670–4678.
13. Sun X, et al. (2008) Nano-graphene oxide for cellular imaging and drug delivery. *Nano Res* 1(3):203–212.
14. Yang X, et al. (2011) Multi-functionalized graphene oxide based anticancer drug-carrier with dual-targeting function and pH-sensitivity. *J Mater Chem* 21(10): 3448–3454.
15. Feng L, Zhang S, Liu Z (2011) Graphene based gene transfection. *Nanoscale* 3(3): 1252–1257.
16. Yuan H, Huang C, Li J, Lykotrafitis G, Zhang S (2010) One-particle-thick, solvent-free, coarse-grained model for biological and biomimetic fluid membranes. *Phys Rev E Stat Nonlin Soft Matter Phys* 82(1 Pt 1):011905.
17. Yuan H, Li J, Bao G, Zhang S (2010) Variable nanoparticle-cell adhesion strength regulates cellular uptake. *Phys Rev Lett* 105(13):138101.
18. Feng L, Liu Z (2011) Graphene in biomedicine: Opportunities and challenges. *Nanomedicine* 6(2):317–324.
19. Yang SH, et al. (2012) Interfacing living yeast cells with graphene oxide nanosheaths. *Macromol Biosci* 12(1):61–66.
20. Qin Z, Buehler M (2012) Bioinspired design of functionalised graphene. *Mol Simul* 38(8-9):695–703.
21. Zhang Y, et al. (2010) Cytotoxicity effects of graphene and single-wall carbon nanotubes in neural phaeochromocytoma-derived PC12 cells. *ACS Nano* 4(6):3181–3186.
22. Mu Q, et al. (2012) Size-dependent cell uptake of protein-coated graphene oxide nanosheets. *ACS Appl Mater Interfaces* 4(4):2259–2266.
23. Titov AV, Král P, Pearson R (2010) Sandwiched graphene—membrane superstructures. *ACS Nano* 4(1):229–234.
24. Guo R, Mao J, Yan L-T (2013) Computer simulation of cell entry of graphene nanosheet. *Biomaterials* 34(17):4296–4301.
25. Brown DM, et al. (2007) An in vitro study of the potential of carbon nanotubes and nanofibres to induce inflammatory mediators and frustrated phagocytosis. *Carbon* 45(9):1743–1756.
26. Sanchez VC, Pietruska JR, Miselis NR, Hurt RH, Kane AB (2009) Biopersistence and potential adverse health impacts of fibrous nanomaterials: What have we learned from asbestos? *Wiley Interdiscip Rev Nanomed Nanobiotechnol* 1(5):511–529.
27. Bao G, Bao XR (2005) Shedding light on the dynamics of endocytosis and viral budding. *Proc Natl Acad Sci USA* 102(29):9997–9998.
28. Gao H, Shi W, Freund LB (2005) Mechanics of receptor-mediated endocytosis. *Proc Natl Acad Sci USA* 102(27):9469–9474.
29. Shi X, Kong Y, Gao H (2008) Coarse grained molecular dynamics and theoretical studies of carbon nanotubes entering cell membrane. *Acta Mech Sin* 24(2):161–169.
30. Shi X, von dem Bussche A, Hurt RH, Kane AB, Gao H (2011) Cell entry of one-dimensional nanomaterials occurs by tip recognition and rotation. *Nat Nanotechnol* 6(11):714–719.
31. Creighton MA, Rangel-Mendez JR, Huang J, Kane AB, Hurt RH (2013) Graphene induced adsorptive and optical artifacts during in vitro toxicology assays. *Small* 9(11): 1921–1927.
32. Xie L, et al. (2011) Graphene nanoribbons from unzipped carbon nanotubes: Atomic structures, Raman spectroscopy, and electrical properties. *J Am Chem Soc* 133(27): 10394–10397.
33. Girit ÇÖ, et al. (2009) Graphene at the edge: Stability and dynamics. *Science* 323(5922):1705–1708.
34. Huang JY, et al. (2009) In situ observation of graphene sublimation and multi-layer edge reconstructions. *Proc Natl Acad Sci USA* 106(25):10103–10108.
35. Warner JH, Schäffel F, Rümmeli MH, Büchner B (2009) Examining the edges of multilayer graphene sheets. *Chem Mater* 21(12):2418–2421.
36. Song B, et al. (2011) Atomic-scale electron-beam sculpting of near-defect-free graphene nanostructures. *Nano Lett* 11(6):2247–2250.
37. Leroy F, Dos Santos DJVA, Müller-Plathe F (2009) Interfacial excess free energies of solid-liquid interfaces by molecular dynamics simulation and thermodynamic integration. *Macromol Rapid Commun* 30(9-10):864–870.
38. Isralewitz B, Gao M, Schulten K (2001) Steered molecular dynamics and mechanical functions of proteins. *Curr Opin Struct Biol* 11(2):224–230.
39. Boal D (2001) *Mechanics of the Cell* (Cambridge Univ Press, Cambridge, UK).
40. Gibson MC, Perrimon N (2003) Apicobasal polarization: Epithelial form and function. *Curr Opin Cell Biol* 15(6):747–752.
41. Madl AK, Pinkerton KE (2009) Health effects of inhaled engineered and incidental nanoparticles. *Crit Rev Toxicol* 39(8):629–658.
42. Delorme-Axford E, Coyne CB (2011) The actin cytoskeleton as a barrier to virus infection of polarized epithelial cells. *Viruses* 3(12):2462–2477.
43. Schäfer C, et al. (2009) One step ahead: Role of filopodia in adhesion formation during cell migration of keratinocytes. *Exp Cell Res* 315(7):1212–1224.
44. Möller W, Hofer T, Ziesenis A, Karg E, Heyder J (2002) Ultrafine particles cause cytoskeletal dysfunctions in macrophages. *Toxicol Appl Pharmacol* 182(3):197–207.
45. Geiser M (2010) Update on macrophage clearance of inhaled micro- and nanoparticles. *J Aerosol Med Pulm Drug Deliv* 23(4):207–217.
46. Duch MC, et al. (2011) Minimizing oxidation and stable nanoscale dispersion improves the biocompatibility of graphene in the lung. *Nano Lett* 11(12):5201–5207.
47. Sasidharan A, et al. (2012) Hemocompatibility and macrophage response of pristine and functionalized graphene. *Small* 8(8):1251–1263.
48. Seong SY, Matzinger P (2004) Hydrophobicity: An ancient damage-associated molecular pattern that initiates innate immune responses. *Nat Rev Immunol* 4(6): 469–478.
49. McEvoy L, Williamson P, Schlegel RA (1986) Membrane phospholipid asymmetry as a determinant of erythrocyte recognition by macrophages. *Proc Natl Acad Sci USA* 83(10):3311–3315.
50. Moyano DF, et al. (2012) Nanoparticle hydrophobicity dictates immune response. *J Am Chem Soc* 134(9):3965–3967.
51. Groot RD, Rabone KL (2001) Mesoscopic simulation of cell membrane damage, morphology change and rupture by nonionic surfactants. *Biophys J* 81(2):725–736.
52. Grafmüller A, Shillcock J, Lipowsky R (2009) The fusion of membranes and vesicles: Pathway and energy barriers from dissipative particle dynamics. *Biophys J* 96(7): 2658–2675.
53. Fedosov DA, Pan W, Caswell B, Gompper G, Karniadakis GE (2011) Predicting human blood viscosity in silico. *Proc Natl Acad Sci USA* 108(29):11772–11777.
54. Li Y, Li X, Li Z, Gao H (2012) Surface-structure-regulated penetration of nanoparticles across cell membrane. *Nanoscale* 4:3768–3775.
55. Yang K, Ma YQ (2010) Computer simulation of the translocation of nanoparticles with different shapes across a lipid bilayer. *Nat Nanotechnol* 5(8):579–583.
56. Cranford S, Buehler MJ (2011) Twisted and coiled ultralong multilayer graphene ribbons. *Model Simul Mater Sci Eng* 19(5):054003.
57. Plimpton S (1995) Fast parallel algorithms for short-range molecular dynamics. *J Comput Phys* 117(1):1–19.
58. Phillips JC, et al. (2005) Scalable molecular dynamics with NAMD. *J Comput Chem* 26(16):1781–1802.
59. Humphrey W, Dalke A, Schulten K (1996) VMD: Visual molecular dynamics. *J Mol Graph* 14(1):33–38, 27–28.
60. Klauda JB, et al. (2010) Update of the CHARMM all-atom additive force field for lipids: Validation on six lipid types. *J Phys Chem B* 114(23):7830–7843.